Int. J. Electrochem. Sci., 15 **(2020)** 9378 – 9391, doi: 10.20964/2020.09.06

International Journal of
ELECTROCHEMICAL
SCIENCE
www.electrochemsci.org

Facile Synthesis of MnO_2@attapulgite Nanoparticles for Supercapacitor

J. Song[1,*], *Y.Z. Song*[1,*], *P. S. Zhao*[1], *X.F. Zhu*[2]

[1] Jiangsu Collaborative Innovation Center of Regional Modern Agriculture & Environmental Protection, School of Chemistry & Chemical Engineering, Huaiyin Normal University, Jiangsu Province Key Laboratory for Chemistry of Low-Dimentional Materials, Jiangsu Key Laboratory for Biomass–based Energy and Enzyme Technology, Huaiyin Normal University, 111 Changjiang West Road, Huaian 223300, Jiangsu Province, PR.China.
[2] National & Local Joint Engineering Research Center for Deep Utilization Technology of Rock-salt Resource, Huaiyin Institute of Technology, Huaian, 223003, Jiangsu Province, PR.China.
[*]E-mail: songjiesj@163.com (J. Song); songyuanzhi@126.com (Y.Z. Song)

Received: 9 May 2020 / *Accepted:* 27 June 2020 / *Published:* 10 August 2020

In this paper the MnO_2@attapulgite nanoparticles have been successfully synthesized for the supercapacitor, and characterized by X-ray diffractometer, scanning electron microscopy, energy dispersive spectrometer, infrared spectrometer, and surface area and pore size analyzers. The cyclic voltammetry and galvanostatic charge/discharge were performed for MnO_2@attapulgite in 1 M Na_2SO_4 aqueous solutions. For the high specific capacitance and long life time the best mass rate of MnO_2: ATP for MnO_2@attapulgite was obtained.

Keywords: MnO_2, attapulgites, supercapacitor

1. INTRODUCTION

Attapulgite (ATP) ($(Mg,Al)_4(Si)_8(O,OH,H_2O)_{26}\cdot nH_2O$), is a natural nano clay that has large specific surface area and high surface activity [1]. The ATP has been used in adhesives, adsorbents, catalysts and catalyst supports due to its one-dimensional fibrous morphology, rapid hydration rate, salt resistance, cation exchange ability and inexpensive cost [2-5].

The metal oxide materials have attracted increasing attention of researchers. Among the metal oxide materials, MnO_2 is one of the most promising applications in supercapacitors because of its high non-toxic, cheap and natural abonundce. MnO_2 has many polymorphs, including α-, β-, γ-, δ-, λ-, ε-crystallographic polymorphs. The nano MnO_2 and MnO_2 composites, such as amorphous MnO_2 on 3D-Ni foam [6] , MnO_2@NiO nanosheets@nanowires hierarchical structures [7], MnO_2 nanosheets

grown on N-doped agaric-derived three-dimensional porous carbon [8], Cobalt hexacyanoferrate/MnO_2 nanocomposite [9], carbon quantum dots anchoring MnO_2/graphene aerogel [10], have been prepared for the supercapacitors. However, the relatively low electrochemical capacitance and life time or expensive cost limits their applications in practical electronic utilization.

In this work, the MnO_2@ATP nanoparticles were prepared and characterized. The supercapacitive behavior of MnO_2@attapulgites in 1M Na_2SO_4 electrolyte was investigated by cyclic voltammetry and galvanostatic charge/discharge techniques.

2. EXPERIMENTAL

The raw ATT (50 g) was dispersed in 200 mL distilled water in an ultrasonic bath for 0.5 h, the bottom sand and large stones were removed, and then the ATP was filtered, washed with distilled water and anhydrous ethanol, respectively. The ATPs were dried in drying oven at 100 ℃ for 24 h. Synthesis of MnO_2@ATP nanoparticles were prepared as follows: 1.0 g $MnSO_4$ powder were dispersed into 10 ml distilled water in a beaker, 0.50 ml concentrated sulfuric acid was dropped into the beaker, and then 1.0 g NaAc, 3.0 g $KMnO_4$ and 0.0～5.0 g ATP were added to the beaker, respectively. The mass of ATP was varied as 0.5, 1.0, 3.0 and 5.0 g, and the obtained products were noted as MnO_2@$ATP_{0.5}$, MnO_2@$ATP_{1.0}$, MnO_2@$ATP_{3.0}$ and MnO_2@$ATP_{5.0}$, respectively. The mixture was treated by 80 W ultrasonic wave for 20 min. The slurry was filtered and repeatedly washed with distilled water and anhydrous ethanol, respectively. The product was dried at 100 ^oC for 24 h.

The morphologies of the prepared products were examined by scanning electron microscopy (SEM), using a QUANTA FEG 450 microscope with an EDAX OCTANE PRO energy dispersive spectrometer (EDS) (USA). The IR spectra were measured by a NICOLET NEXUS470 spectrometer (USA) in the frequency range 4000–400cm^{-1}. X-Ray diffraction (XRD) analysis was performed on the as-prepared products with Switzerland ARL/X/TRA X-ray diffractometer rotating anode with Cu-Ka radiation source (l = 1.540562 Å). The nitrogen adsorption and desorption experiments were carried out at 77 K by means of SA3100 surface area and pore size analyzers (USA).

The mixing the active material, carbon black and polyvinylidene fluoride (PVDF) were taken in the weight ratios of 80:10:10. The mixture was first formed to slurry by adding ethyl alcohol, then coated on platinum net with an apparent area of 1 ×1 cm, and finally dried under at 100 ℃ for 3 h. The loading mass of active material was about 0.5～2 mg cm^{-2} . The prepared electrodes were impregnated with a 1 M Na_2SO_4 aqueous solution for 1h before the electrochemical tests. The electrochemical characterization of the as-prepared MnO_2@ATP electrodes was also carried out with a CHI660e electrochemical analyzer (CHI, USA) in a three-electrode cell system. The prepared electrode, a 10 cm graphite rod in diameter of 0.5 cm and an Ag/AgCl, 3 M KCl electrode were used as working, counter and reference electrodes, respectively. The electrochemical impedance spectroscopy (EIS) was measured at the open-circuit potential over the frequency range of 10^5 to 0.01 Hz with an a.c. amplitude of 5 mV. Land-CT2001A battery analyzer (Wuhan, China) was also performed for the charge/discharge cycling life tests of MnO_2@ATP nanoparticles [11, 12].

3. RESULTS AND DISCUSSION

3.1 Nitrogen adsorption/desorption isotherms and BJH pore-size distribution

As shown in Fig. 1, the isotherm of the MnO_2@ATP nanoparticles is classified as type IV according to the IUPAC classification, indicating a typical mesoporous material with relatively uniform channel-like pores. The specific surface area (SSA) was calculated using the Brunauere Emmette-Teller (BET) method for MnO_2@ATP. The pore-size distributions (PSDs) were calculated by the Barrette Joynere Halenda (BJH) plots using the nitrogen desorption isotherm. As shown in Fig. 1 inset and Table 1, the PSD of ATP nanoparticles narrow center was found at 50 and 104 nm, while the peaks of PSD for MnO_2 appeared at around 59 and 113 nm. The peaks of PSDs for MnO_2@ATP changed slightly in the range of 46～56 and 106～111 nm. The SSA of ATP, MnO_2 and MnO_2@ATP calculated by BET method is 188, 106 and 157～170 m^2 g^{-1}, respectively. Compared with MnO_2, the SSA values of MnO_2@ATP were more than that of the MnO_2 but less than that of ATP.

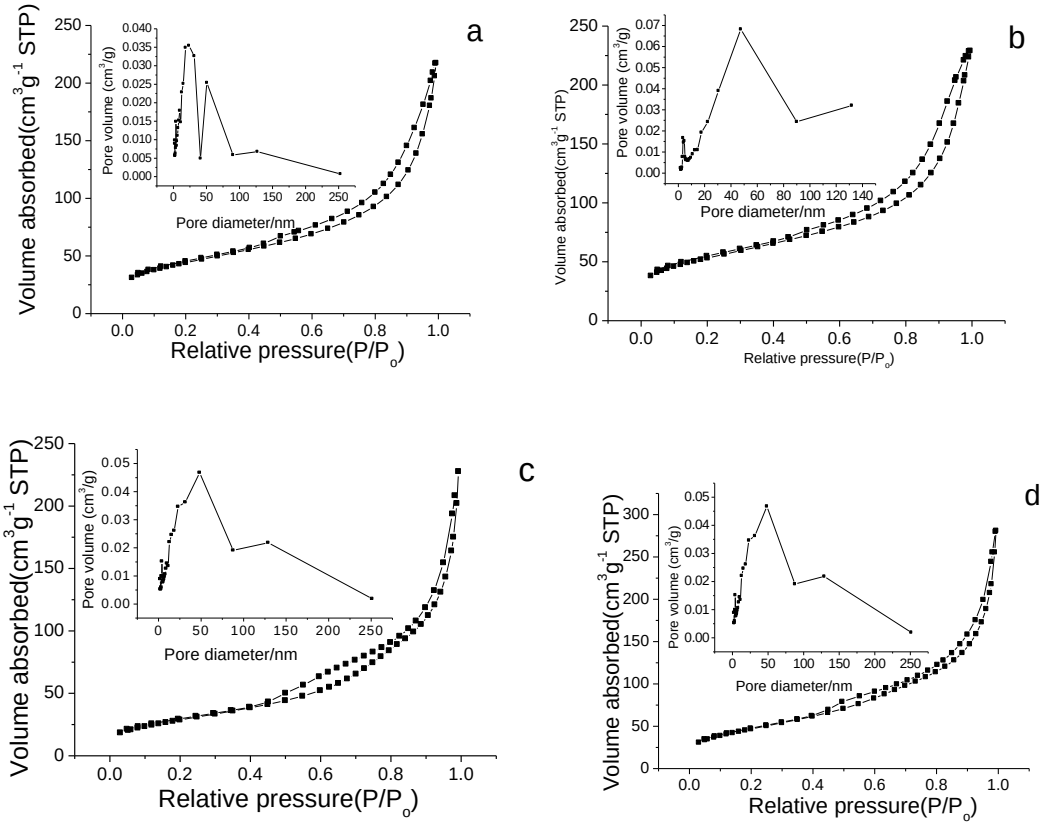

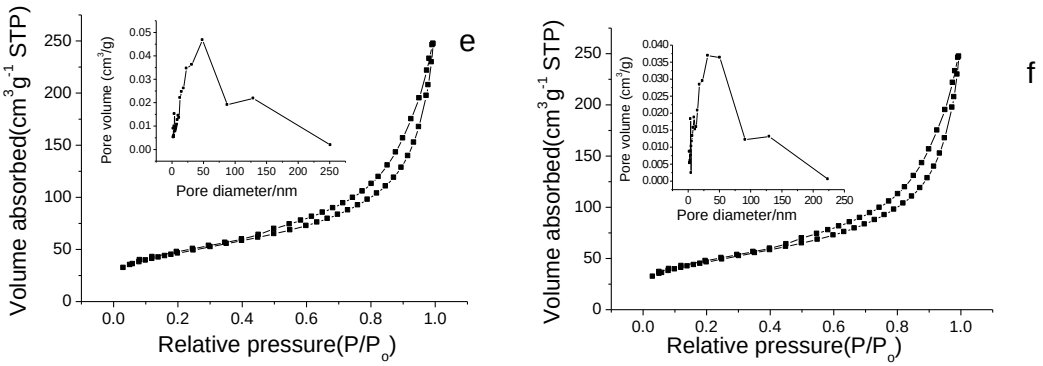

Figure 1. Nitrogen adsorption/desorption isotherms and BJH pore-size distribution of curves (inset) of MnO_2@ATP nanoparticles (a: ATP; b: MnO_2; c: MnO_2@$ATP_{0.5}$; d: MnO_2@$ATP_{1.0}$; e: MnO_2@$ATP_{3.0}$; f: MnO_2@$ATP_{5.0}$)

Table 1. PSD and SAA of MnO_2, ATP and MnO_2@ATP

	ATP	MnO_2	MnO_2@ $ATP_{0.5}$	MnO_2@ $ATP_{1.0}$	MnO_2@ $ATP_{3.0}$	MnO_2@ $ATP_{5.0}$
PSD (nm)	46,105	58, 114	53,110	60,104	48,110	47,108
SAA(m^2 g^{-1})	188	106	170	166	160	157

3.2 Micrographs of materials

Fig. 2 shows the SEM micrographs and EDS of the ATP, MnO_2 and MnO_2@ATP nanoparticles. The nano rods ATP, the honeycomb MnO_2 and MnO_2@ATP nanoparticles were observed. The EDS pattern and element analysis showed that the elements of Si, Al, Mg, Mn, K and O in ATP were found, indicating that K^+ ions were absorbed by MnO_2. While except K, Mn and O, the elements the Al and Mg in MnO_2@ATP were also found.

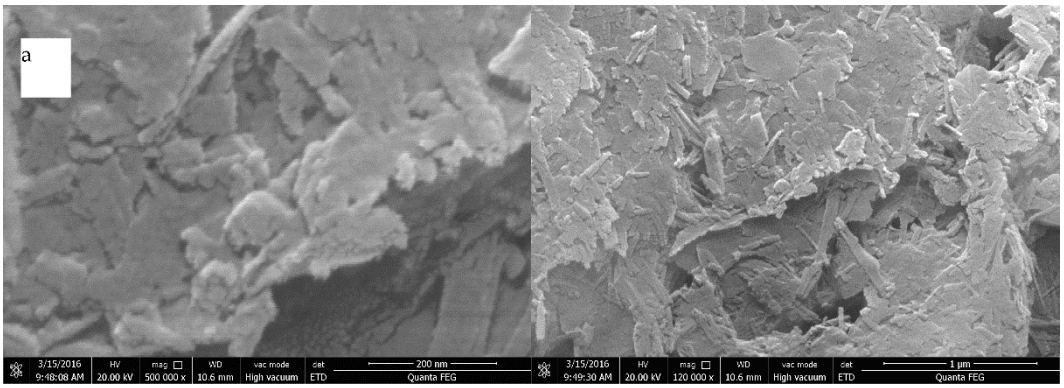

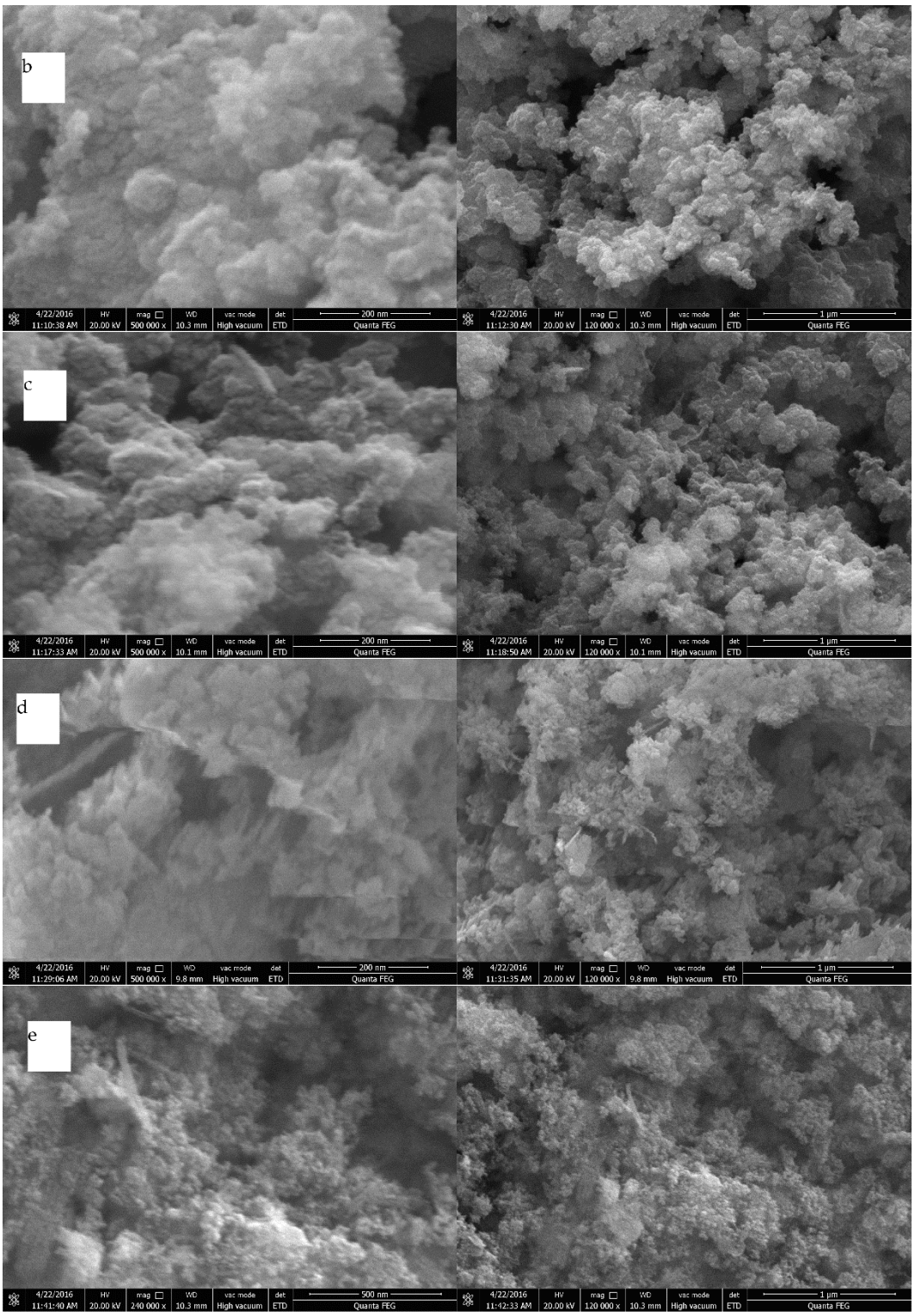
b
4/22/2016 11:10:38 AM HV 20.00 kV mag 500 000 x WD 10.3 mm vac mode High vacuum det ETD 200 nm Quanta FEG
4/22/2016 11:12:30 AM HV 20.00 kV mag 120 000 x WD 10.3 mm High vacuum ETD 1 µm Quanta FEG
c
4/22/2016 11:17:33 AM HV 20.00 kV mag 500 000 x WD 10.1 mm High vacuum ETD 200 nm Quanta FEG
4/22/2016 11:18:50 AM HV 20.00 kV mag 120 000 x WD 10.1 mm High vacuum ETD 1 µm Quanta FEG
d
4/22/2016 11:29:06 AM HV 20.00 kV mag 500 000 x WD 9.8 mm High vacuum ETD 200 nm Quanta FEG
4/22/2016 11:31:35 AM HV 20.00 kV mag 120 000 x WD 9.8 mm High vacuum ETD 1 µm Quanta FEG
e
4/22/2016 11:41:40 AM HV 20.00 kV mag 240 000 x WD 10.3 mm High vacuum ETD 500 nm Quanta FEG
4/22/2016 11:42:33 AM HV 20.00 kV mag 120 000 x WD 10.3 mm High vacuum ETD 1 µm Quanta FEG

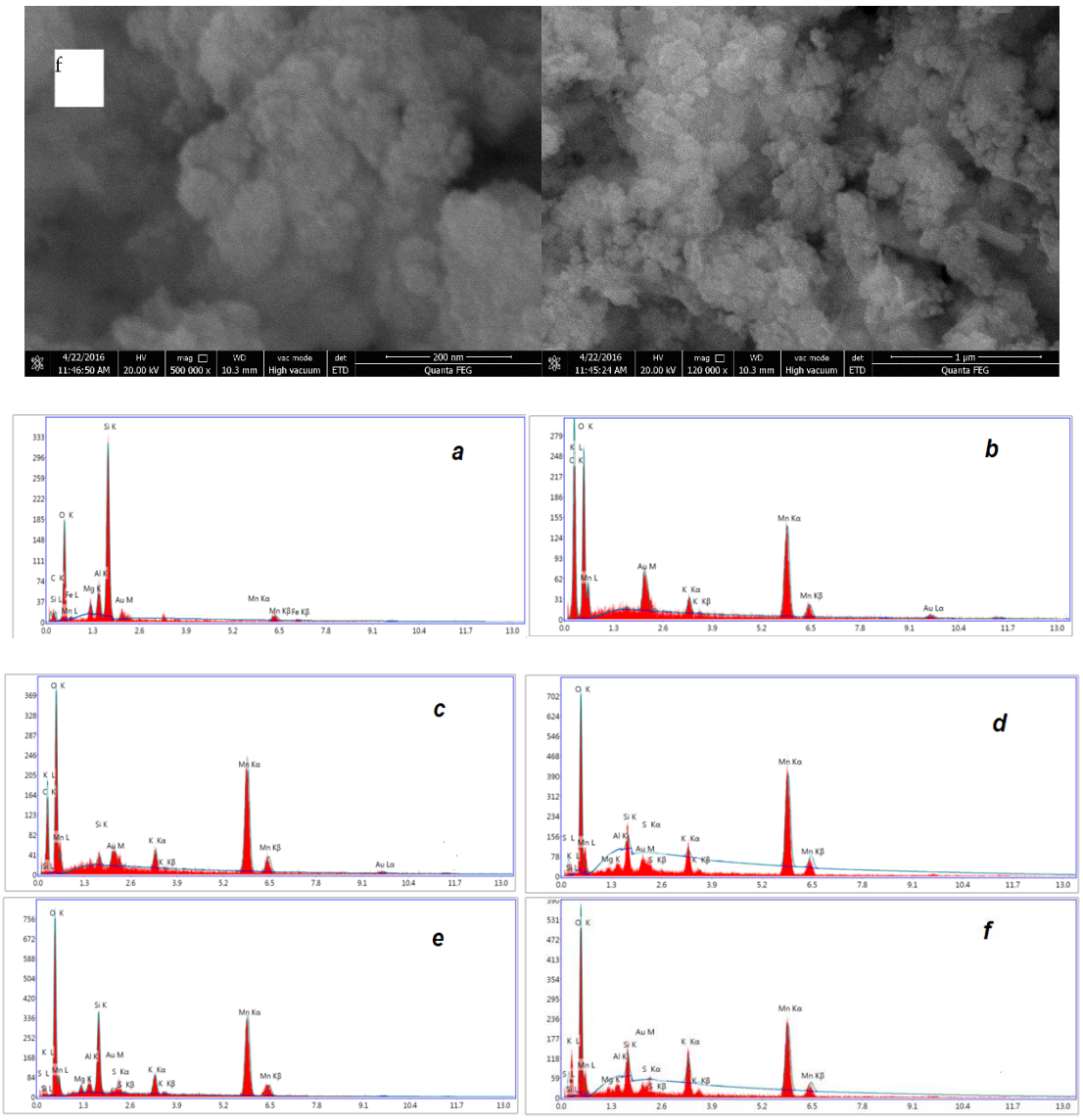

Figure 2. SEM images and EDS of ATP (a), MnO_2 (b), MnO_2@$ATP_{0.5}$ (c), MnO_2@$ATP_{1.0}$ (d), MnO_2@$ATP_{3.0}$ (e) and MnO_2@$ATP_{5.0}$ (f).

3.3 XRD pattern of ATP and MnO_2@ATP

The XRD patterns of natural ATP clay, the MnO_2@ATP nanocomposite are shown in Fig. 3. As for the ATP clay, the characteristic peaks are found to locate at 8.5°, 13.6°, 20.0°, 27.1°, and 35.8° correspond to the primary diffraction of (110), (200), (040), (231), and (161) reflections for the ATP, which matches well with palygorskite crystal structure (JCPDS file (PDF No. 05-0099)) and the literature [13]. The interlayer distance of the typical peak observed at 8.5° can be attributed to the basal plane of the ATP framework. The peaks at 13.6°, 16.5°, and 20.0° represent the Si-O-Si crystalline layers in ATP [13-15].

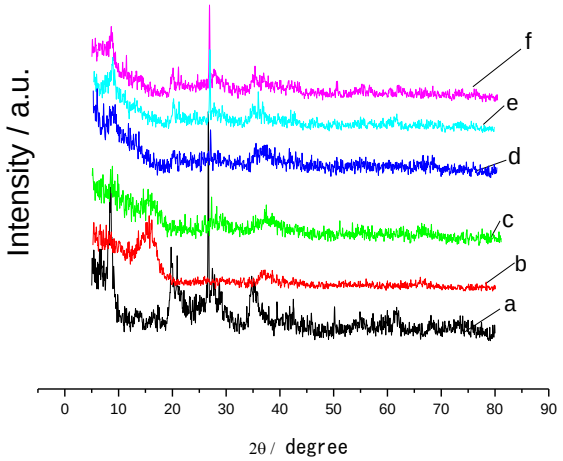

Figure 3. XRD pattern of ATP (a), MnO_2 (b), MnO_2@$ATP_{0.5}$ (c), MnO_2@$ATP_{1.0}$ (d), MnO_2@$ATP_{3.0}$ (e) and MnO_2@$ATP_{5.0}$ (f).

A broad diffraction peak of MnO_2 and MnO_2@$ATP_{0.5}$ was found at 16 °, which did not match the crystalline compound, and the peak of MnO_2@$ATP_{1.0}$ at 16 ° disappeared. Except the peaks originating from the ATP two diffraction peaks appear at 2θ = 37.5° and 2θ = 65.1°, respectively, which can be indexed to tetragonal α-MnO_2 (JCPDS NO. 44-0141) and consistent with the priors work [16].

3.4 IR spectra of ATP and MnO_2@ATP

The IR spectra of ATP and MnO_2@ATP nanoparticles are shown in Fig.4. For ATP, the band at 3536 and 3388 cm^{-1} was attributed to the stretching vibration of hydroxyl groups of octahedral magnesium and the tetrahedral silicon [17]. The band at 1657 and 1030 cm^{-1} were attributed to the asymmetric stretching of -OH and Si–O–Si group, respectively.

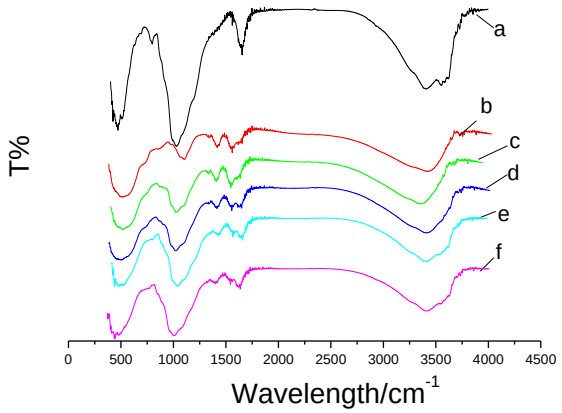

Figure 4. IR spectra of ATP (a), MnO_2 (b), MnO_2@$ATP_{0.5}$ (c), MnO_2@$ATP_{1.0}$ (d) MnO_2@$ATP_{3.0}$ (e) and MnO_2@$ATP_{5.0}$ (f).

The peaks 3437 cm^{-1} for MnO_2 ascribe to stretching of –OH of absorbed H_2O, and the peaks of 1551, 1426, 1081 could be assigned to the stretching of O–Mn. The peaks at 3437 and 1081 MnO_2 in MnO_2@ATP shifted to red direction, indicating that the ~~the~~ system energy of MnO_2@ATP decreases, and the ATP and MnO_2 formed novel stable composite adsorbents.

3.5 Cyclic voltammetry (CV) and Charging and discharging of battery

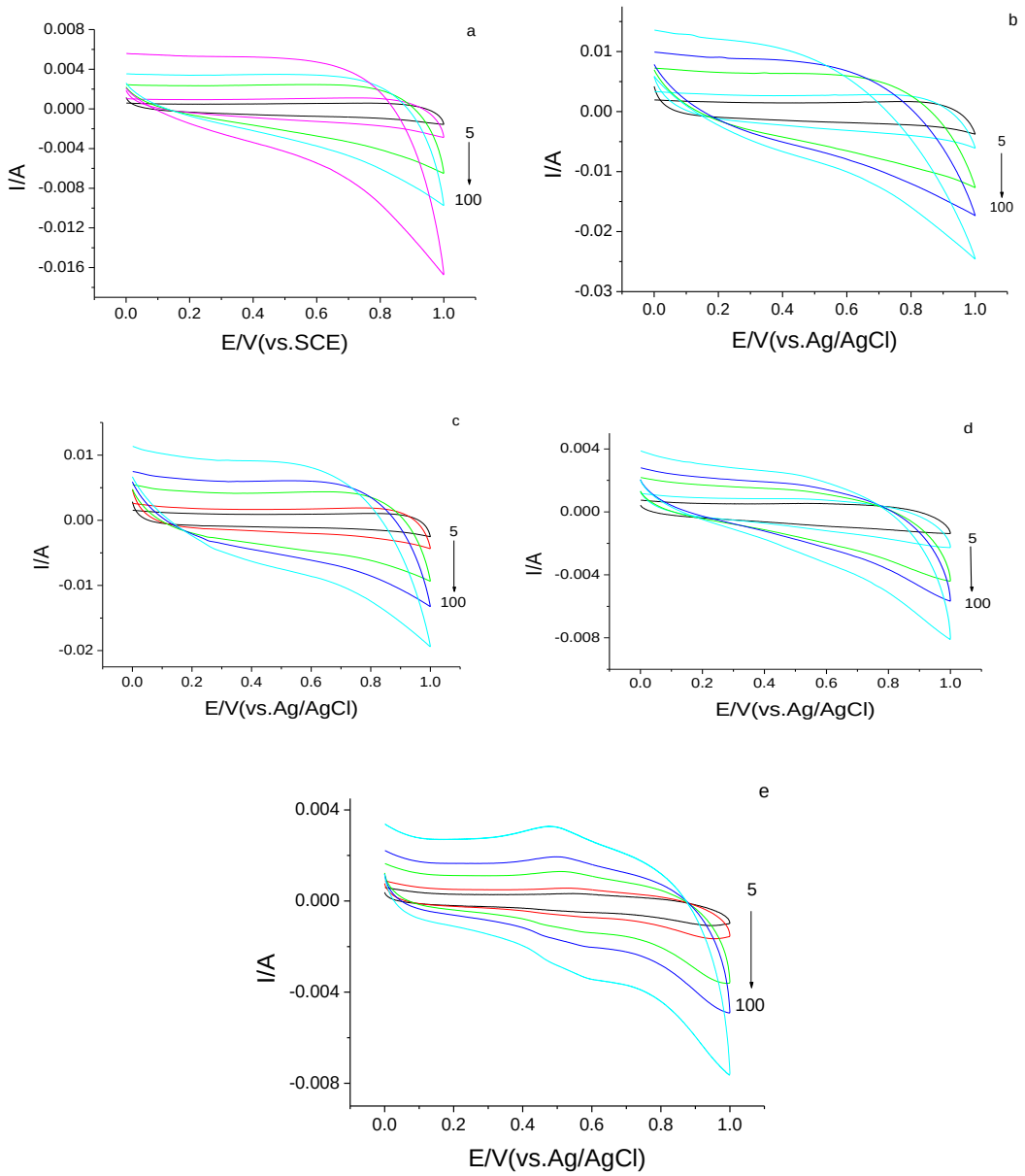

Figure 5. CV curves of ATP (a), MnO_2 (b), MnO_2@$ATP_{0.5}$ (c), MnO_2@$ATP_{1.0}$ (d) MnO_2@$ATP_{3.0}$ (e) and MnO_2@$ATP_{5.0}$ (f), at scan rates of 5, 10, 30, 50 and 100 mV/ s

The MnO_2@ATP nanoparticles were characterized with cyclic voltammetry and galvanostatic charge/discharge (GC) in 1 M Na_2SO_4 aqueous solutions in a fixed voltage window of 0～1.00 V vs.

Ag/AgCl. Fig. 5 shows the CV curves of sample MnO_2@ATP nanoparticles at the scan rate of 5～100 mV s^{-1}.

Galvanostatic charge/discharge curves are shown in Fig.6. The specific capacitance (SC) obtained with CV and discharge curves are calculated using the equation of $SC = \frac{1}{2mv\Delta V}\int idV$ [18] and $SC = \frac{it}{m\Delta V}$, respectively **[**19**].** The calculated SC values of MnO_2 and MnO_2@ATPs are summarized in Table 2. The SC values of MnO_2@$ATP_{1.0}$ are more than that of MnO_2, other MnO_2@ATP and many previous literatures [20-24].

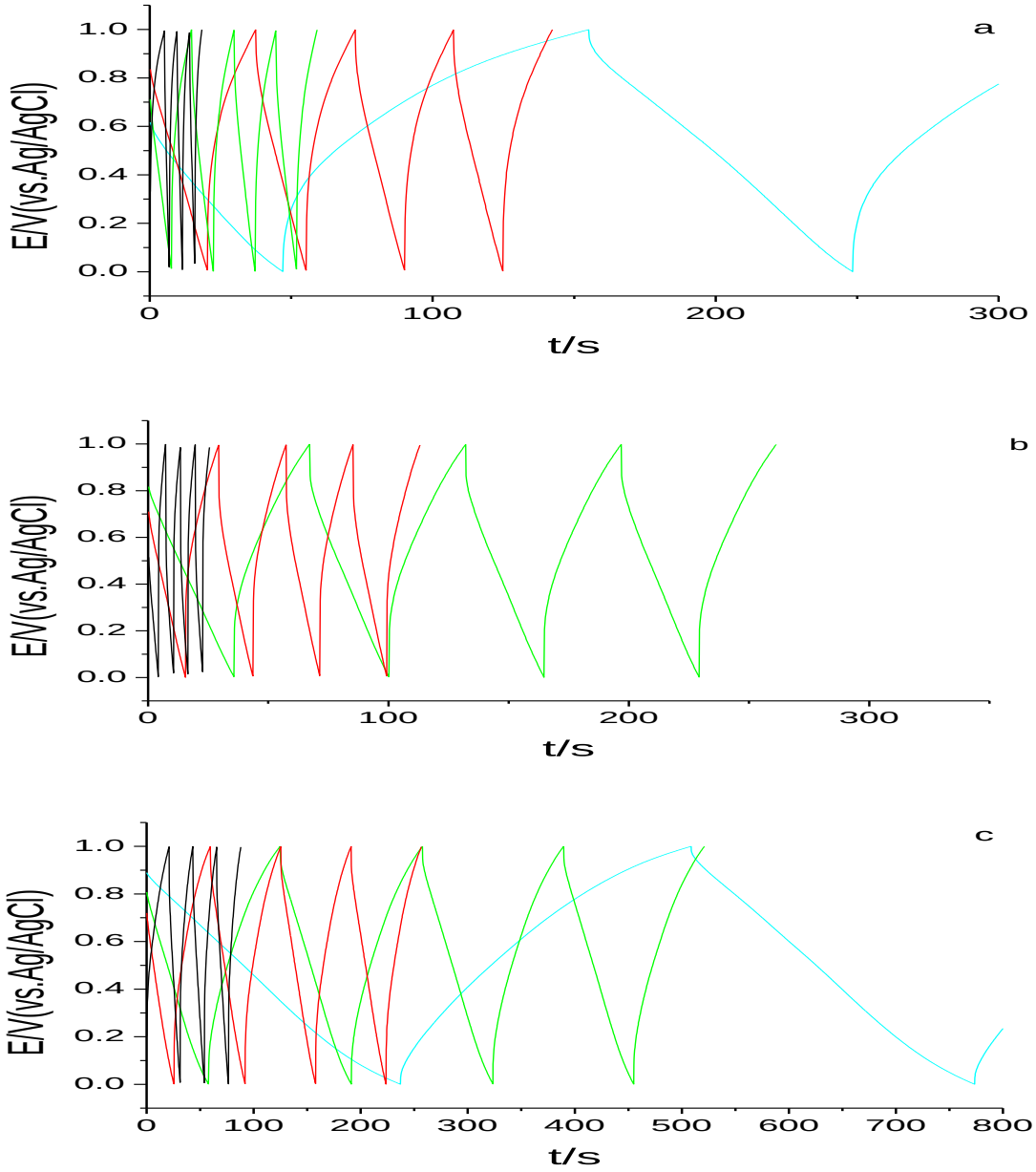

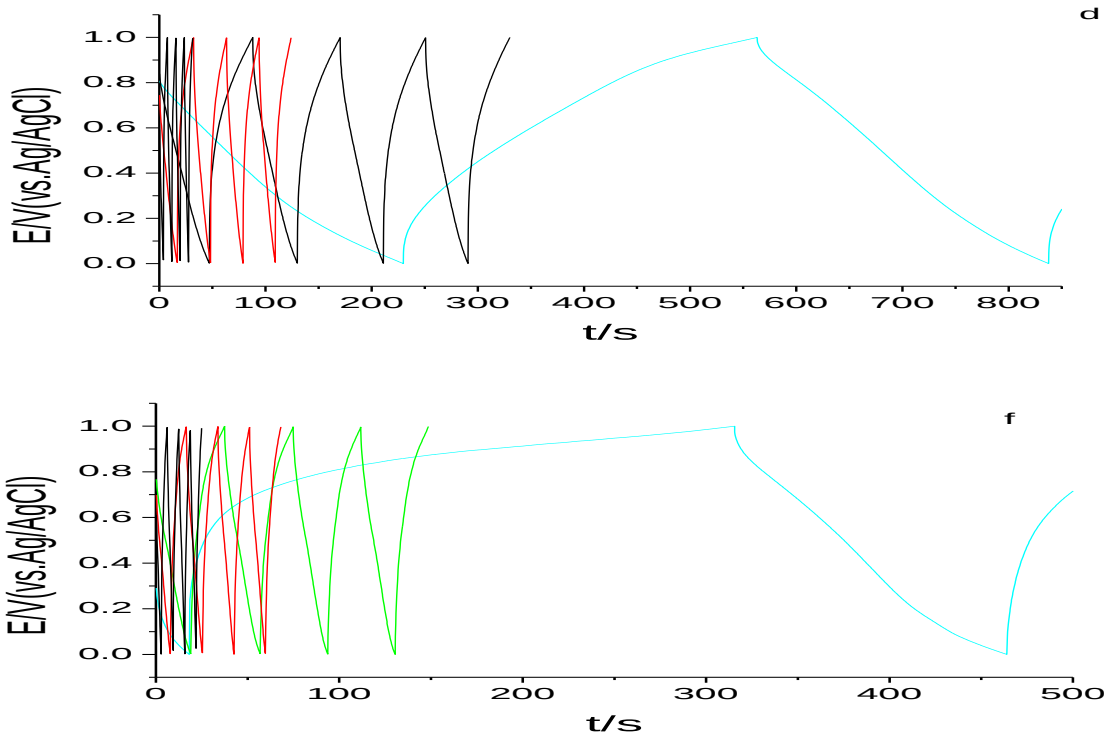

Figure 6. Galvanostatic charge/discharge curves of ATP (a), MnO_2 (b), MnO_2@$ATP_{0.5}$ (c), MnO_2@$ATP_{1.0}$ (d) MnO_2@$ATP_{3.0}$ (e) and MnO_2@$ATP_{5.0}$ (f)

Table 2. Comparison of the SC values of MnO_2 and MnO_2@ATPs with other materials

Material	GC(A/g)				CV(mV/s)				
	1	3	5	10	5	10	30	50	100
Nanoplate-MnO_2 composites [20]					308.5				
Graphene/wrapped honeycomb MnO_2 [21]			147						
MnO_2/activated carbon nanotube [22]					250				
MnOx NPs [23]			146.3						
Nitrogen-doped grapheme-ultrathin MnO_2 sheet [24]	290								
MnO_2[This work]	92.2	45.6	30.6	18.5	216.2	183.0	136.3	113.4	83.7
MnO_2@$ATP_{0.5}$[This work]	149.0	103.2	71.8	30.1	334.5	274.7	182.2	130.2	75.8
MnO_2@$ATP_{1.0}$[This work]	249.9	206.2	164.0	111.3	496.2	418.9	309.3	240.3	163.6
MnO_2@$ATP_{3.0}$[This work]	278.3	125.4	82.0	34.6	376.2	250.8	140.3	99.0	69.0
MnO_2@$ATP_{5.0}$[This work]	149.5	55.4	44.0	28.7	215.6	165.0	111.7	97.5	79.8

3.6 EIS and cycling stabilities of battery

As shown in Fig.7, the EIS of the MnO_2 and MnO_2@ATP nanoparticles are composed of a partially overlapped semicircle and a straight sloping line. It can be seen that the Faradic charge transfer resistances (Rct) decrease with the increasing of ATP masses, according to the equivalent circuit the R_{ct} of MnO_2, MnO_2@$ATP_{0.5}$, MnO_2@$ATP_{1.0}$, MnO_2@$ATP_{3.0}$ and MnO_2@$ATP_{5.0}$ is 32, 19, 14, 10, and 3 Ω, respectively. The small Rct values and the mesoporous networks constructed with nanoscale particles lead the electrolyte efficiently flood into the pores of the network structure and decrease the polarization of the electrode, resulting in the increase of its specific capacitance. Due to the obvious decrease of MnO_2 in MnO_2@$ATP_{5.0}$ the composition and structure affect the penetration of the Na_2SO_4 and ion reaction area. As results, the lower specific capacitance and high R_{ct} were obtained.

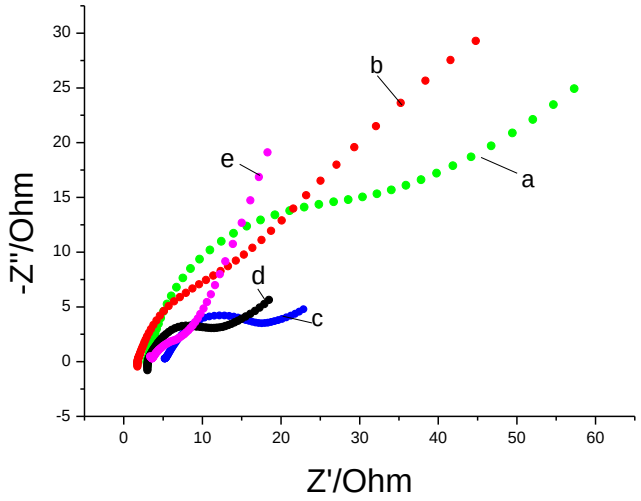

Figure7. EIS of ATP (a), MnO_2 (b), MnO_2@$ATP_{0.5}$ (c), MnO_2@$ATP_{1.0}$ (d) MnO_2@$ATP_{3.0}$ (e) and MnO_2@$ATP_{5.0}$ (f)

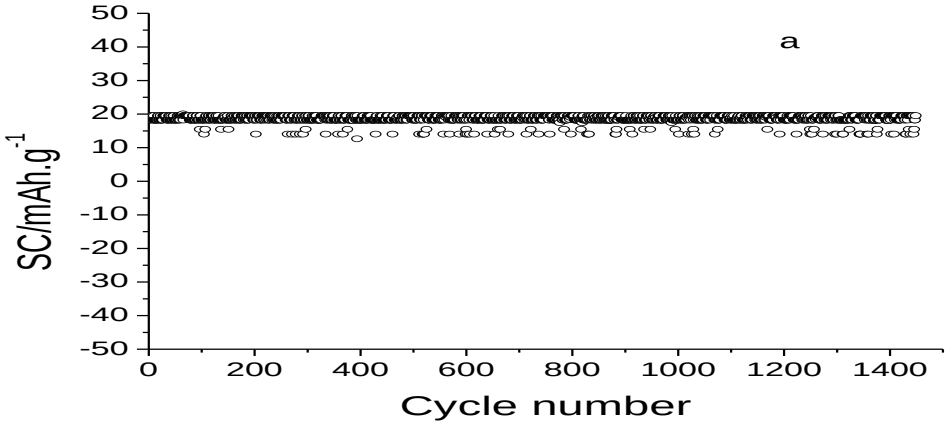

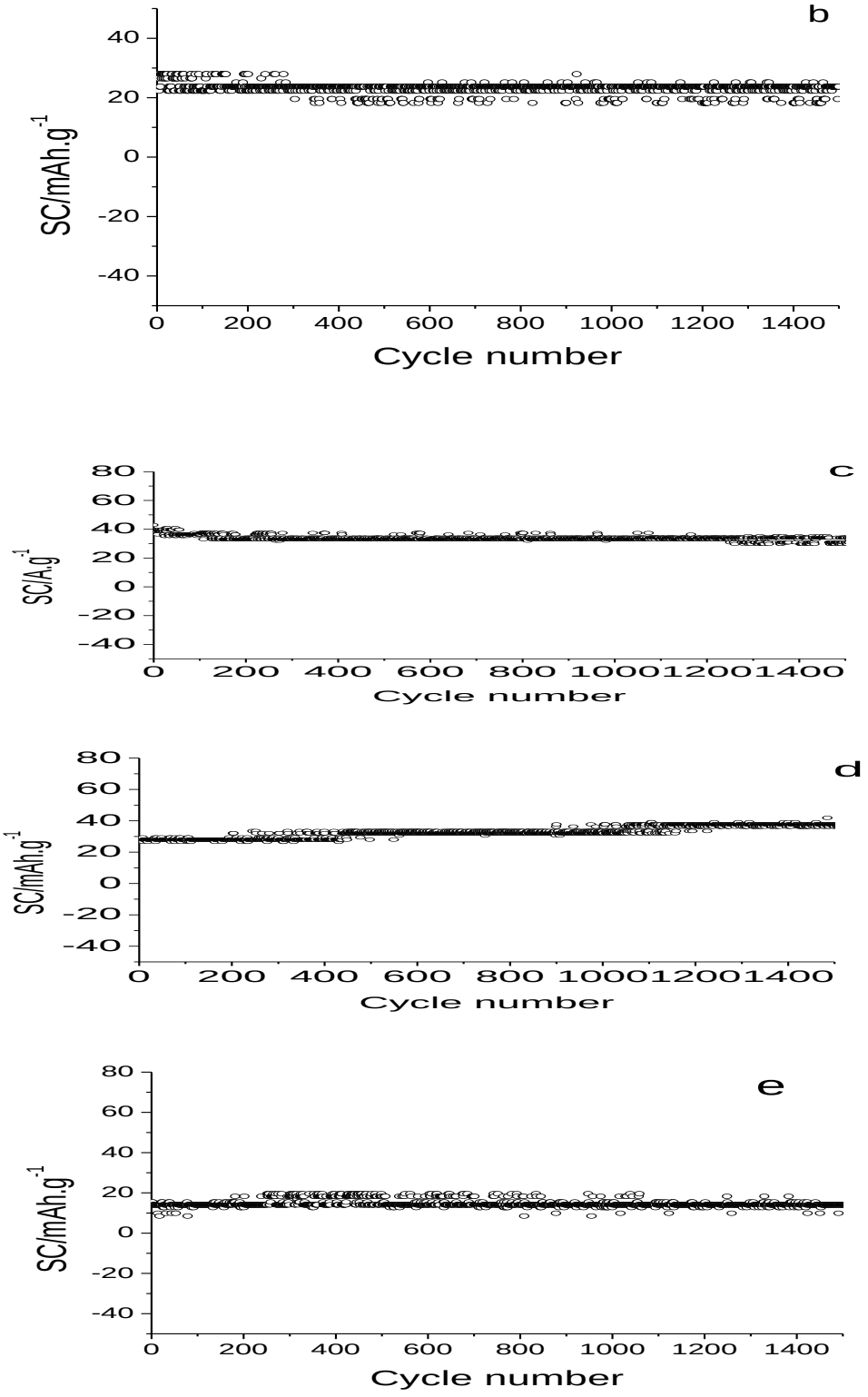

Figure 8. Charge/discharge cycling life of ATP (a), MnO_2 (b), MnO_2@$ATP_{0.5}$ (c), MnO_2@$ATP_{1.0}$ (d), MnO_2@$ATP_{3.0}$ (e) and MnO_2@$ATP_{5.0}$ (f) at current density of 5A/g.

The data of cycling stability are shown in Fig.8, the cycling stabilities of MnO_2@ATP nanoparticles were evaluated at a current density of 5A g^{-1} for 1500 cycles. The SC values of

MnO_2@$ATP_{1.0}$ are more stable and more than those of others due to the good fabrication, indicting that the high and stable SC values were controlled by the mass rate of ATP: MnO_2.

4. CONCLUSION

In this paper the MnO_2@ATP nanoparticles were fabricated. The MnO_2@$ATP_{1.0}$ nanoparticles showed a distinctly improved electrochemical performance. The improved rate performance and good cycling stability make it as a promising electrode material for supercapacitors.

ACKNOWLEDGEMENT
The authors gratefully acknowledge the financial support of The Research Foundation of Huaiyin Normal University (HSXT2-313), the National Natural Science Foundation of China (51602118), and the Open Science Foundation for Jiangsu Province Key Laboratory for Chemistry of Low-Dimentional Materials (Grant No. JSKC17009).

References

1. L. Zhu, J. Guo, and P. Liu. *Appl. Clay Sci*., 119(2016)87.
2. Z. H. Duan, Q. N. Zhao, S. Wang, Z. Yuan, Y, J. Zhang, X. Li, Y. W.Wu, Y. D. Jiang, H. L.Tai. *Sensor Actuat B-Chem.*, 305(2020)127534.
3. Y. Wang, R. S. Zhou, C. Z. Wang, G. Z. Zhou, C. Y. Hua, Y. Y. Cao，Z. Z. Song. *J Alloy Compd.*, 817(2020)153286.
4. F. L. Yang, J. S. Weng, J. J. Ding, Z. Y. Zhao, L. Z. Qin, F. F. Xia. *Renew Energ.*, 151(2020)829.
5. W. Cheng, C. Ding, Y. Sun, X. Wang. *Chem. Eng. J.*, 269(2015)1.
6. T. Y. Fang, Y. Z. Zeng, Y. C. Liu, W. D. Yang.*J Mater Sci: Mater Electron*, 31(2020)**7**672.
7. X. L. Zhao, X. Y. Liu, F. Li, M. Huang. *J Mater Sci.*, 55(2020)2482.
8. D. Y. Li, J. Lin, Y. Lu, Y. Huang, X. He, C. Yu, J. Zhang, C. C. Tang. *J Alloy Compd.*, 815(2020) 152344.
9. Z. X. Song, W. Liu, Q. Zhou, L. Zhang, Z. Zhang, H. D. Liu, J. Q. Du, J. L. Chen, G. C. Liu, Z. F. Zhao. *J. Power Sources*, 465 (2020) 228266.
10. H. P. Lv, Y, Yuan, Q. J. Xu, H. M. Liu, Y. G. Wang, Y. Y. Xia. *J. Power Sources*, 398(2018)167.
11. Y.Z. Song, R.X. Zhao, K.K. Zhang, J.J. Ding, X.M. Lv, M. Chen, J.M. Xie. *Electrochim Acta*, 230(2017)350.
12. J. J. Zhu, L. L. Yu, J.T. Zhao. *J Power Sources*, 270(2014)411.
13. Q. Zhou, Q. Gao, W. Luo, C. Yana, Z. Ji, P. Duan. *Colloid Surface A*, 470(2015)248.
14. X. Li, Z. Zong, W. Ma, Z. Wei, Y. Li, J. Cao, M. Mayyas, Zh. Li, X. Wei. *Fuel Process Technol.*, 131(2015) 376.
15. X. Li, D. Zhang, X. Liu, L. Shi, L. Sun. *Chem.Eng. Sci*., 141(2016)184.
16. Y. Pan, Z. Mei, Z. Yang, W. Zhang, B. Pei, H. Yao. *Chem. Eng. J.*, 242(2014)397.
17. Q.H. Fan, X.L. Tan, J.X. Li, X.K. Wang, W.S. Wu, G. Montavon. *Environ. Sci.Technol*., 43(2009)5776.
18. D.P. Dubal, R. *Holze. Energy*, 51(2013)407.
19. J. W. Lee, A S Hall, J Kim, T. E. Mallouk. *Chem. Mater.*, 24(2012)1158.
20. H. Huang, X. Wang. *Nanoscale*, 3(2011)3185.
21. J. Zhu, J. He. ACS *Appl. Mater. Interfaces*, 4(2012)1770.
22. J. M. Ko, K. M. Kim. *Mater. Chem. Phys.*,114(2009) 837.

23. W. Xiao, D. Hu, C. Peng, G. Z. Chen. ACS *Appl. Mater. Interfaces*, 3(2011)3120.
24. S. Yang, X. Song, P. Zhang, L. Gao. ACS *Appl. Mater. Interfaces,* 5(2013)3317.